Journal of Imaging Science and Technology® 53(6): 060201–060201-10, 2009.

Statics and Dynamics of Carrier Particles in Two-Component Magnetic Development System in Electrophotography

Hiroyuki Kawamoto▲ and Takashi Hiratsuka
Department of Applied Mechanics and Aerospace Engineering, Waseda University, 3-4-1 Okubo, Shinjuku, Tokyo 169-8555, Japan
E-mail: kawa@waseda.jp

Abstract. *The authors used a simple model and a prototype machine to study statics and dynamics of a magnetic brush in a two-component development system in electrophotography. In the model experiment, the authors measured the normal and tangential forces of the brush formed from a chain of magnetic carrier particles when it comes in contact with the photoreceptor to clarify the relationship between the tangential friction force and the diameter of the carrier particles, magnetic flux density, and the length of the brush. The tangential friction force increased with the magnetic flux density and decreased with an increase in the length of the brush; however, the total force was unaffected by the diameter of the carrier particles. On the other hand, numerical calculations performed using an improved distinct element method revealed that although the total force was not affected by the diameter of the carrier particles, the individual differential force acting on the magnetic particles of the chain was small, and the density of the carrier particles that come in contact with the photoreceptor drum was high when the size of the particles was small. In the investigation carried out using the prototype machine, it was found that the magnetic brush formed in the development area is inclined in a direction parallel to the magnetic field and that the chains are crushed by the photoreceptor drum. Although the total pressure applied on the photoreceptor was almost independent of the diameter of the carrier particles, the differential force exerted by individual chains is small and distributes dense when the size of the particles is small; on the other hand, it is large and distributes rough when the size of the particles is large as predicted by the model investigation. This result suggests that small carrier particles are advantageous in preventing any disturbances in the images developed on the photoreceptor. The effects of the development gap and the thickness of the layer of supplied carrier particles have also been evaluated. © 2009 Society for Imaging Science and Technology.*
[DOI: 10.2352/J.ImagingSci.Technol.2009.53.6.060201]

INTRODUCTION

Statics and dynamics of magnetic particles in a magnetic field are of great interest in magnetic brush development systems that are adopted in color and/or high-speed electrophotography machines.[1–3] A magnetic brush is used to develop electrostatic latent images on a photoreceptor drum, as shown in Figure 1. Magnetic carrier particles with electrostatically attached toner particles are introduced in the vicinity of a rotatory sleeve that encloses a stationary magnetic roller. The diameter of carrier particle is on the order of several tens of micrometers and that of a toner particle is approximately 10 μm. The magnetized carrier beads form chain clusters, the so-called brush, on the sleeve in the magnetic field, as shown in Fig. 1. The tips of chains touch the photoreceptor surface in the development area, and the toner particles on the chains move toward the electrostatic latent images created by a laser beam on the photoreceptor to form real images. The brush plays an important role in this development system for achieving high-quality printing. Sufficient density and moderate brush force are required to obtain a satisfactory image density and also to prevent image defects. Therefore, it is necessary to clarify the relationship between the kinetic characteristics of the formed brush and the design parameters such as the diameter of the carrier particles, magnetic flux density, and the development gap.

From this point of view, experimental, theoretical, and numerical studies have been conducted on the magnetic interaction between magnetic particles. To clarify statics of magnetic particles in a magnetic field, Paranjpe and Elrod[4] expressed the interaction force between magnetic dipoles and the determined chain configuration on the basis of the principle of magnetic potential energy minimization. However, since they assumed a simple row of particles in a straight line, the calculated results were fundamental and could not simulate the actual complex brush shown in Fig. 1. We carried out a numerical simulation by the distinct

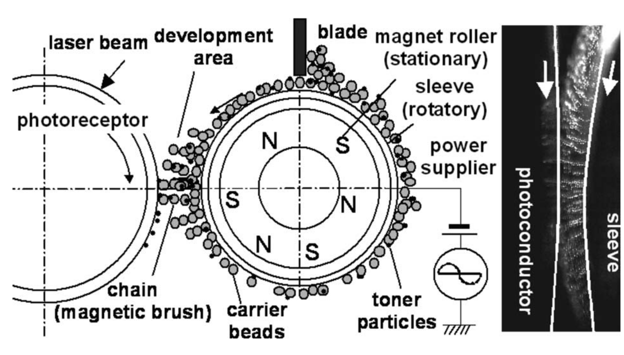

Figure 1. Schematic drawing of two-component magnetic brush development system in electrophotography (left) and photograph of magnetic brush in development area (right).

▲IS&T Member.

Received Mar. 9, 2009; accepted for publication Jul. 28, 2009; published online Oct. 8, 2009.
1062-3701/2009/53(6)/060201/10/$20.00.

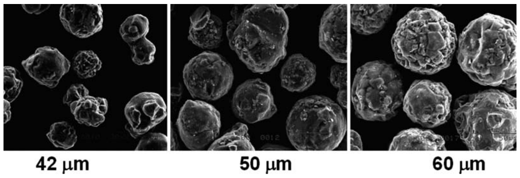

Figure 2. Scanning electron microscope photographs of carrier particles used for experiment.

element method (DEM) based on Paranjpe's formulation to clarify the mechanism of chain formation and to determine the configuration of the three-dimensional brush,[5] the lateral stiffness of the chain, and the resonant frequency of the chain vibration.[6] We also carried out model experiments with a solenoid coil for generating the magnetic field; the results agreed reasonably well with the results of the numerical calculation. However, the experiments were fundamental and could not simulate the actual system; this was because the experiments were carried out under the assumption that the brush was not in contact with the photoreceptor. Furthermore, brush formation was restricted to a magnetic flux density of less than 10 mT owing to Joule heating.

In this study, the statics and dynamics of the magnetic brush have been investigated in two steps. In the first step, a fundamental investigation is conducted to clarify the relationships between the tangential friction force acting on the brush when it is in contact with the photoreceptor and the diameter of the carrier particles, magnetic flux density, and the length of the brush. Then, the dynamic behavior of the brush is observed in an actual developer using a high-speed microscope camera, and the experimental results are confirmed by numerical simulations carried out using the improved DEM, in which periodic boundary conditions are imposed for improving the development system.

FUNDAMENTAL INVESTIGATION

Carrier Particles and Magnetic Field

Spherical soft magnetic carrier particles were used for the experiment. The toner particles were not mixed with the carrier particles because the investigation was concentrated on the magnetic effect. Toner particles must be mixed with the carrier particles for investigating toner dynamics and some image defects such as ghost, toner scattering, and bead-carry-out. We are conducting these investigations, and these will be reported in separate papers. The magnetic carrier particles were made of soft ferrite and had average diameters of 42 (±4), 50 (±5), and 60 (±6) μm (± standard deviation); their volume density and relative magnetic permeability were 2200 kg/m^3 and 3.9, respectively. Scanning electron micrographs (SEM) of these carrier particles are shown in Figure 2.

Instead of the actual magnetic roller, a permanent plate magnet (Nd-Fe-B, ϕ33.8 mm/T4.8 mm, NEOMAX) was used to generate the magnetic field. As shown in Figure 3 (left), the magnetic flux density can be controlled by the gap between the magnet and the positioning stage on which the carrier particles are mounted. The axial magnetic flux density with respect to the gap is shown in Fig. 3 (right).

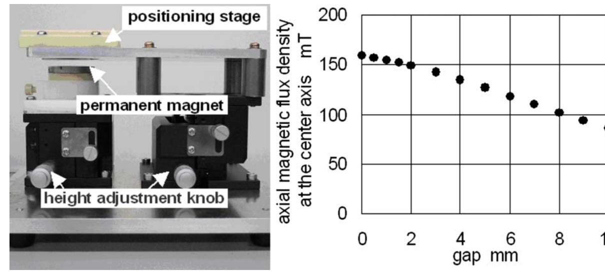

Figure 3. Experimental setup for the formation of magnetic brushes (left) and axial magnetic flux density along the center axis (right).

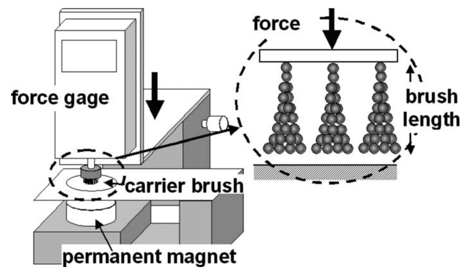

Figure 4. Experimental setup for measuring normal reaction force.

Normal Force

The normal force exerted on the pseudophotoreceptor surface was measured using the setup shown in Figure 4. A 0.2-mm-thick plate with a hole 10 mm in diameter was set on the positioning stage located far above the permanent magnet, and 50 mg of the carrier particles was filled in the hole. Then, the positioning stage was brought near the permanent magnet to obtain a chain of carrier particles, and the normal reaction force was measured using a force gauge (ZP-2N, Imada). The bulk density of the carrier particles was adjusted to suit the typical operating conditions of an actual instrument.

Two parametric experiments were conducted. In one experiment, the normal reaction force was measured for different lengths of brush at a constant magnetic flux density of 130 mT. In the other, the normal reaction force was measured for different magnetic flux densities at a constant brush length of 0.6 mm. The experimental results in the former case are marked as "measured (normal)" in Figure 5. As expected, the normal reaction force increased with the compression of the brush because the bulk density of carrier particles increased in the compressed condition of the brush. On the other hand, the normal reaction force was almost independent of the diameter of the particles.

Experimental results obtained at a constant brush length are marked "measured (normal)" in Figure 6. The normal reaction force increased with the magnetic flux density owing to the increased magnetic force of attraction between the carrier particles in strong magnetic field. However, the normal reaction force was almost independent of the diameter of the particles, as in the case of the constant magnetic flux density shown in Fig. 5, although the normal reaction force measured for the 42-μm particles was smaller than that for the 50- and 60-μm particles.

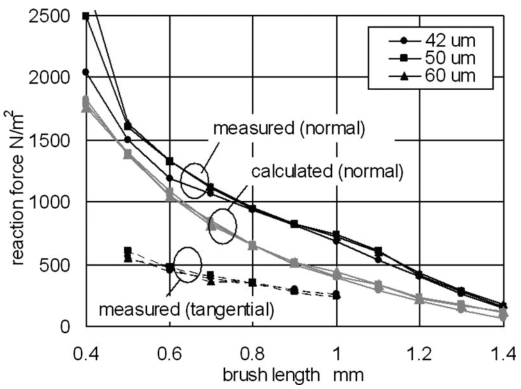

Figure 5. Relationship between length of brush and reaction force in magnetic flux density of 130 mT.

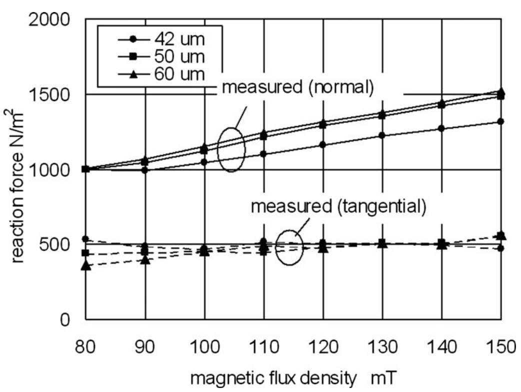

Figure 6. Relationship between magnetic flux density and reaction force at a constant brush length of 0.6 mm.

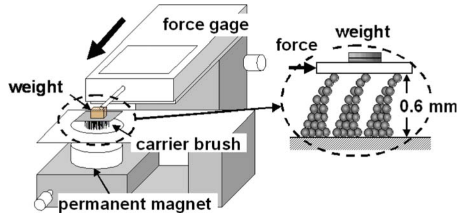

Figure 7. Experimental setup for measuring tangential reaction force.

Tangential Force

The force tangential to the pseudophotoreceptor plate was measured using the setup shown in Figure 7. The procedure used for forming the magnetic brush was the same as that for the measurement of the normal reaction force. After the brush was formed, a small aluminum plate (dimensions: $14\times14\times0.2$ mm^3) and a weight were placed on the brush, and the tangential reaction force was applied by the force gage from the lateral side of the weight. The brush length was adjusted by using the weight. Since the tangential reaction force increased almost linearly with the lateral displacement of the force gage and saturated beyond a displacement of 1.5 mm, the force at the point of displacement at 1.5 mm in the lateral direction was considered to be the tangential reaction force.

Two parametric experiments similar to those used for measuring the normal reaction force were conducted. In one experiment, the tangential reaction force was measured for different brush lengths at a constant magnetic flux density of 130 mT. In the other, the tangential reaction force was measured for different magnetic flux densities at a constant brush length of 0.6 mm. The experimental results in the former case are marked as “measured (tangential)” in Fig. 5. The characteristics of the tangential reaction force were similar to those of the normal reaction force, i.e., the tangential force increased with the depression of the brush and was almost independent of the diameter of the particle. The ratio of the tangential force to the normal force was 0.35–0.38, irrespective of the length of the brush and the diameter of the particle. The ratio was assumed to be the friction coefficient between the brush and the aluminum plate.

Experimental results obtained when the brush length was maintained constant are marked as “measured (tangential)” in Fig. 6. The characteristics of the tangential reaction force were similar to those of the normal reaction force. The tangential reaction force increased with the magnetic flux density and was almost independent of the diameter of the particles as in the case of the constant magnetic flux density. The ratio of the tangential force to the normal force was 0.35–0.4, irrespective of the magnetic flux density and the diameter of the particle; this ratio was almost identical to that obtained at constant magnetic flux density, thereby, supporting the hypothesis that this ratio is the friction coefficient between the brush and the aluminum plate.

Procedure for Numerical Calculation

Numerical simulations based on the three-dimensional DEM were performed to calculate the differential reaction force exerted by the magnetic brush on the aluminum plate.[7] Details of the numerical simulation are described in Appendix. The procedure for the numerical calculations was similar to the experimental procedure. Before application of the magnetic field, the carrier particles were allowed to fall freely from a height of 2 mm to the surface of the positioning stage, wherein they were distributed in an area of dimensions 2×2 mm^2. The positions on the stage where the particles remained stationary were determined to be their initial positions so that the results conformed with those of the actual experiments. The toner particles were not mixed with the carrier particles as the same reason described in the previous section. Particle diameters were assigned randomly to each particle; however, the distributions of the diameter of the carrier particles were coincided with the actual measurements. Then, the magnetic field was applied gradually in a direction normal to the plate. After the magnetic flux density was increased to 130 mT at the surface of the positioning stage, a virtual plate placed on the brush was moved toward the stage, as shown in Figure 8, and the normal force exerted by the compressed brush on the plate was calculated. The constants used for the numerical calculation are as follows:

(a) Young’s modulus of the carrier particles: 10^3 MPa.
(b) Poisson’s ratio of the carrier particles: 0.35.
(c) Friction coefficient between the particles: 0.45.
(d) Number of polygonal angles of the carrier particles for the estimation of rolling friction coefficient: 12.

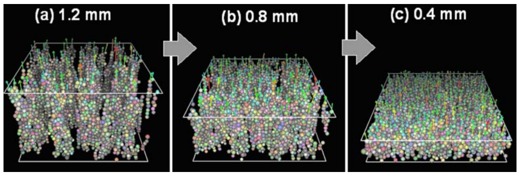

Figure 8. Numerical method for estimation of the normal reaction force exerted by the compressed magnetic brush.

(e) Damping coefficient between particles based on Voigt model: 0.6.
(f) Relative magnetic permeability of carrier particles: deduced from the B-H curve, which is nonlinear with respect to the magnetic flux density.
(g) Young's modulus of the stage and the plate: 5×10^4 MPa.
(h) Poisson's ratio of the stage and the plate: 0.3.
(i) Friction coefficient between the particles and the stage/plate: 0.35.

The number of 42-, 50-, and 60-μm particles used in the DEM was 13,700, 7,870, and 4,420, respectively. The time step of the calculation was 2×10^{-8} s; however, the magnetic interaction was calculated at intervals of 5×10^{-6} s. The magnetic interaction force was calculated within a spherical region whose diameter was eight times the particle. These conditions and simplifications were justified by a numerical method.

Results and Discussion

The calculated normal reaction force calculated for different lengths of brush is marked as "calculated (normal)" in Fig. 5. The calculated and measured normal reaction forces had similar characteristics, though the former had a smaller value, i.e., the force increased with the depression of the brush and was almost independent of the diameter of the particles.

Figure 9 shows the distributions of differential forces exerted by the magnetic particle chains that were in contact with the plate. The vectors in the figure indicate the magnitude and direction of the tangential forces. The number density of the chains in contact with the plate was high and the differential reaction force was small when the carrier particles were small. The averaged interval between the particles was deduced from Fig. 9 and is summarized in Figure 10. This interval is obtained from the formula as $l/\sqrt{n}$, where n is the number of chains in $l\times l$ area.[7] It is evident that the chains are dense when the particles are small. This feature was confirmed by our experiment. Images of the top view of the magnetic brushes are shown in Figure 11 (top); and the averaged intervals between the magnetic particles were deduced by the same method used in the numerical calculation (graph in Fig. 11). Since the measured intervals were for the free brush and not the compressed brush, a direct comparison between the measured and calculated values could not be made. However, magnetic particle chains were dense when the particles were small both in the experiment and in the numerical simulation.

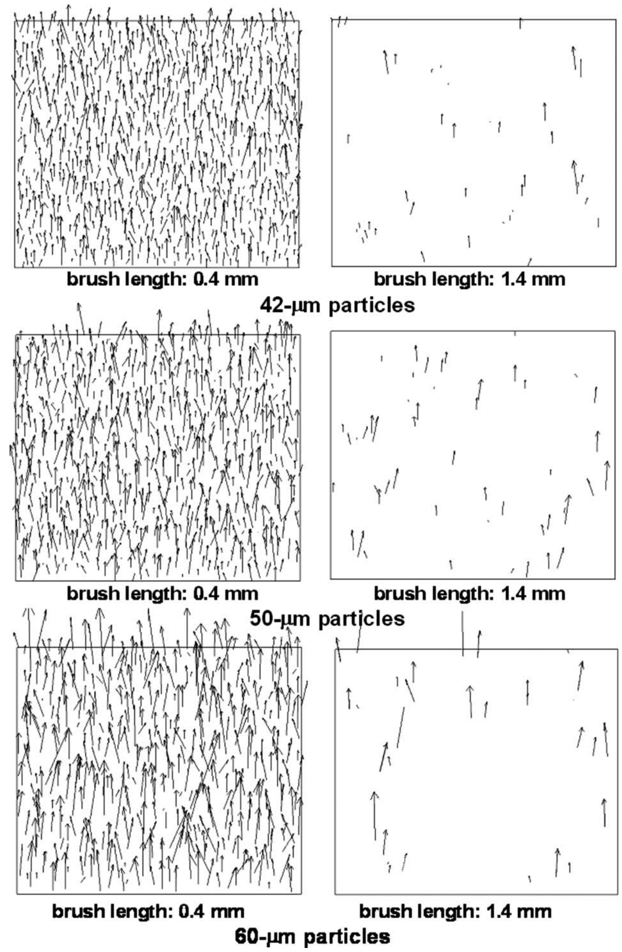

Figure 9. Calculated distribution of the carrier particles that came in contact with the plate and the normal reaction force exerted by the magnetic brush on 2×2 mm^2 plate in magnetic flux density of 130 mT.

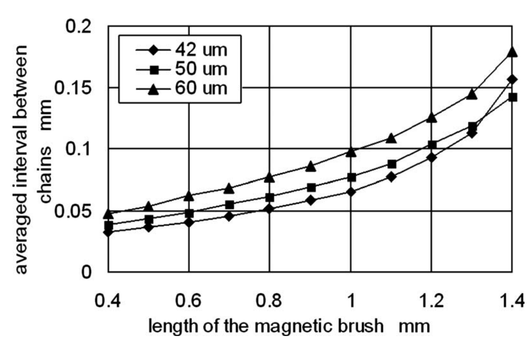

Figure 10. Calculated interval between the particles at different lengths of brush in magnetic flux density of 130 mT.

Figure 12 summarizes the calculated results of the density of the carrier particles in contact with the plate and the averaged differential force exerted by the individual carrier particles at a brush length of 0.4 mm and a magnetic flux density of 130 mT. It is clear that the chains are dense when the particles are small; however, the differential force was small when the particles were small. Since the total pressure applied to the plate is the product of the chain density and the differential force, the total force is independent of the diameter of the carrier particles. This hypothesis is sup-

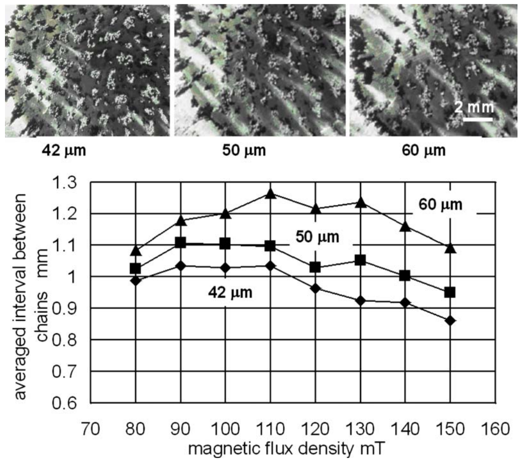

Figure 11. Measured interval between free chains for various values of magnetic flux density and diameter of carrier particles.

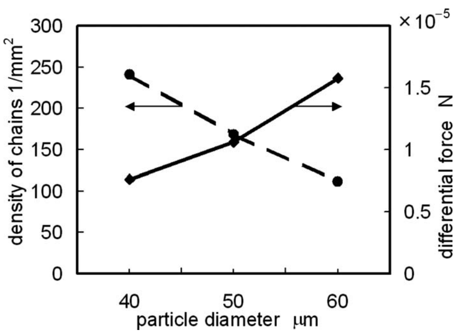

Figure 12. Calculated carrier particle density and averaged force exerted by individual carrier particles at a brush length of in magnetic flux density of 130 mT.

ported by the experimental results, according to which the total reaction force exerted by the brush on the plate is almost independent of the diameter of the carrier particles.

DYNAMICS IN THE DEVELOPMENT SYSTEM

Since the actual development system is not as simple as the simplified model adopted in the fundamental investigation, dynamics of the brush were observed and calculated for a prototype machine that simulated the actual development system.

Experimental Setup

Figure 13 shows the schematic representation of the experimental setup used for the observation of the dynamic characteristics of the magnetic particle chains in the development area. The prototype machine was used for the experiment instead of a commercial printer. The diameters of the drum and the sleeve were 100 mm and 25 mm, respectively. The drum and the sleeve were rotated at 29 and 219 rpm (revolutions per minute), respectively. The development gap, which is the minimum gap between the drum and sleeve, was fixed at 400 μm. The drum was not coated with a photoconductive film and, thus, a bare aluminum drum without any insulative coating was used. The voltage was not applied between the drum and the sleeve so as to

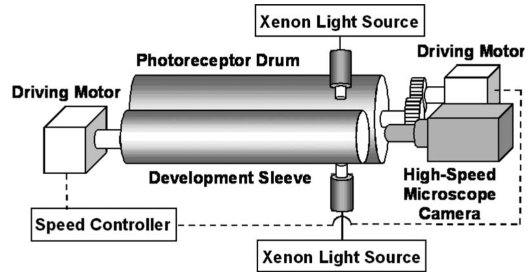

Figure 13. Experimental setup for observation of dynamic behavior of chains in the development area by using high-speed microscope camera.

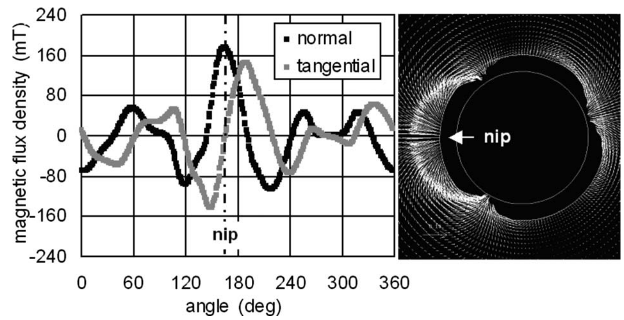

Figure 14. Measured distribution of the magnetic flux density on the sleeve surface (left) and estimated magnetic flux density around the sleeve (right).

eliminate the effect of the electrostatic force. The dynamic behavior of the chains was observed with a high-speed microscope camera (Photoron, Fastcam-max 120 K model 1) placed to the right-hand side of the development gap.

The carrier particles used for the experiment were similar to those used for the fundamental investigation cited above. The toner particles were not mixed with carrier particles as in the case of fundamental investigation.

The magnetic field generated by the magnetic roller was estimated using the magnetic flux density measured at the sleeve surface; for this measurement, the magnetic dipoles were assumed to be distributed on the roller, and the two-dimensional distribution of the magnetic flux density was calculated by superposing the magnetic flux density generated at each dipole. Figure 14 shows the measured distribution of the magnetic flux density on the sleeve and the estimated magnetic flux density around the sleeve. The distribution of the estimated magnetic flux density was in qualitative agreement with the observed profile of the brush in the vicinity of the development gap, as shown in Figure 15.

Results and Discussion

Observation and Calculation of Brush Dynamics

Figure 16 shows calculated and observed behavior of the brush in the development area. The calculation was carried out in a domain that extended to a length of 1 mm in the longitudinal direction, and it is assumed that this narrow domain arrays periodically in the axial longitudinal direction. First, particles are allowed to fall freely on the sleeve, and once the particles become stationary on the sleeve, the sleeve is rotated gradually to the rated speed. The total num-

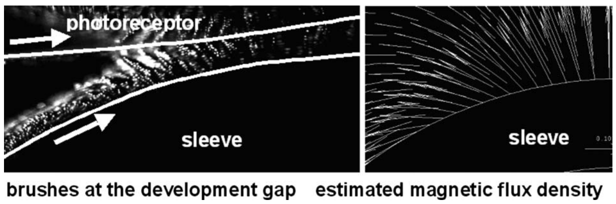

Figure 15. Observed profile of brushes (left) and estimated magnetic flux density (right) in the vicinity of the development gap. Chains are directed to flux lines.

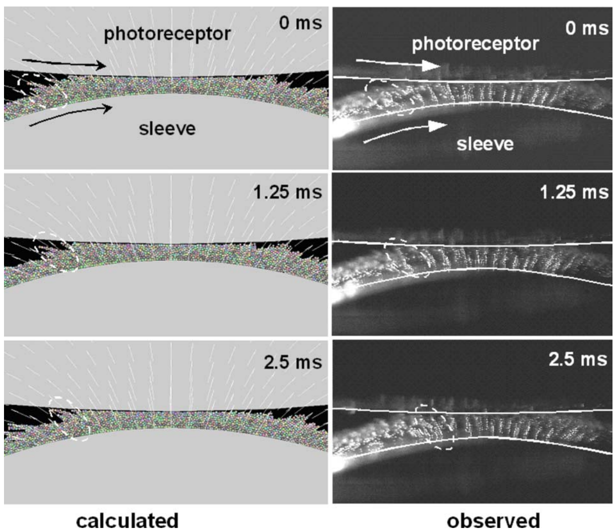

Figure 16. Calculated and observed behavior of chains at development gap.

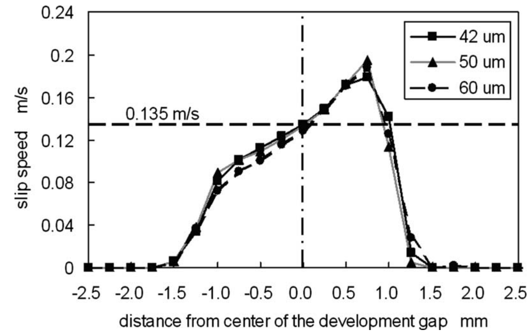

Figure 17. Calculated slip speed of chains in contact with the photoreceptor drum. Relative speed of the photoreceptor drum and the sleeve is 0.135 m/s (parameter: diameter of carrier particles).

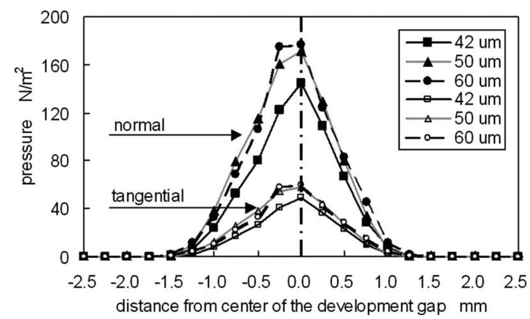

Figure 18. Calculated normal and tangential pressure exerted by the chains on the photoreceptor drum (parameter: diameter of carrier particles).

ber of 60-μm particles used for the numerical calculation is 12,300. This number is consistent with the actual volume density of carrier particles fed into the development area. Not only the chain formation but also the slip speed, pressure, and bulk density are evaluated by the calculation.

First of all, it was confirmed that the calculated result agreed reasonably well with the observed profile of the brush. Chains were formed almost parallel to the magnetic flux lines shown in the figures on the left. At the initial stages of chain formation, chains were inclined to the sleeve and gradually returned to their normal states when they approached the development gap. Then the chains came in contact with the photoreceptor drum and were compressed by the drum. The chains swept the drum in this condition. The chains became free again at the back of the development area and inclined again toward the flux lines. These characteristics were well recognized both in the DEM results and experimental observations.

Effect of Diameter of the Carrier Particles

Figure 17 shows the calculated slip speed of the chains that came in contact with the photoreceptor drum. The time-averaged values are plotted in the figure. The slip speed is low before the chains reach the center of the development gap; at the center, the slip speed becomes equal to the relative speed of the photoreceptor drum and the sleeve (0.135 m/s), and then, it becomes higher than the relative speed when the chains leave the development area. Finally, the chains become free after they exit the gap. These features imply that the brush is depressed to backward before the center and spring just before the chains become free. The spring-back of the chains behind the development area appears to cause stripe defects of the developed toner images on the photoreceptor if the force exerted by the brush on the photoreceptor is very high. In any case, the slip speed is independent to the diameter of the carrier particles.

Figure 18 shows the calculated normal and tangential pressures exerted by the brush on the photoreceptor drum. The time-averaged data are plotted in the figure. The ratio of the normal pressure to the tangential pressure is approximately 0.35, which coincides with the friction coefficient between the photoreceptor and the carrier particles. The pressures are also almost irrelevant to the diameter of the carrier particles. However, unlike the distribution of the slip speed, the distribution of the pressures is almost symmetric with respect to the distance from the center of the development gap.

To realize sufficient image density and to prevent image defects due to the friction force, the pressure must be moderate. If the pressure is too low, a sufficient number of toner particles are not developed; on the other hand, if the pressure is too high, a stripe defect is developed on the photoreceptor.

Figure 19 shows the averaged density of the particles that come in contact with the photoreceptor, and Figure 20 shows the differential distribution of the normal pressure

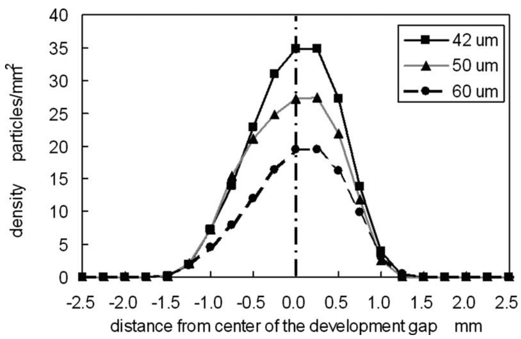

Figure 19. Density of particles that come in contact with photoreceptor (parameter: diameter of carrier particles).

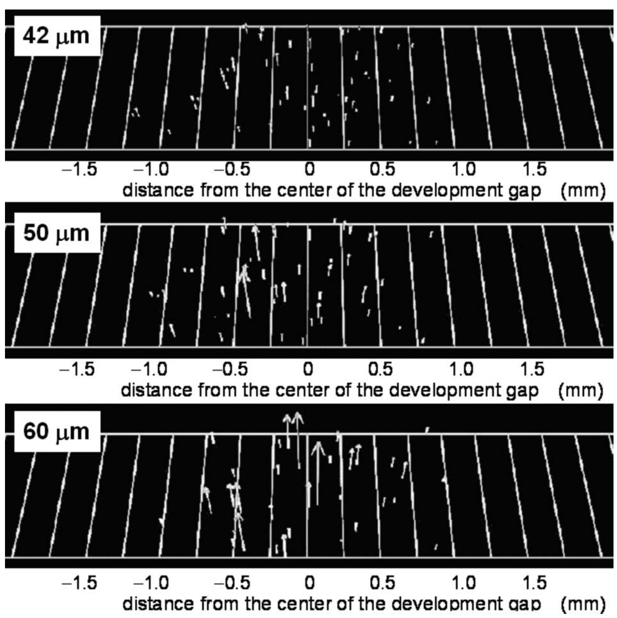

Figure 20. Differential distribution of the normal pressure exerted on the photoreceptor. The tangential pressure is 0.35 times the normal pressure.

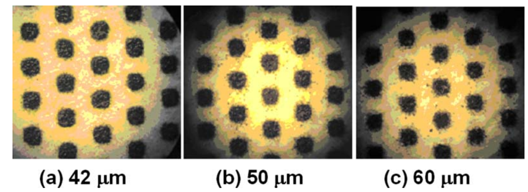

Figure 21. Photograph of printed dot images.

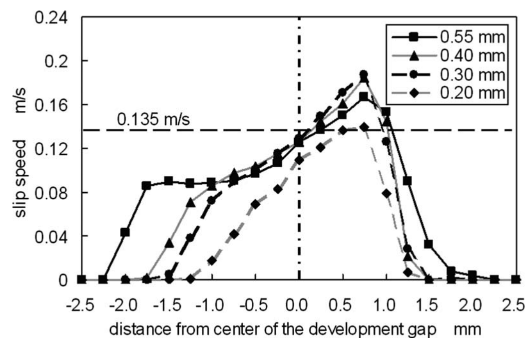

Figure 22. Calculated slip speed of the brush that comes in contact with the photoreceptor drum (parameter: thickness of the layer of supplied carrier particles).

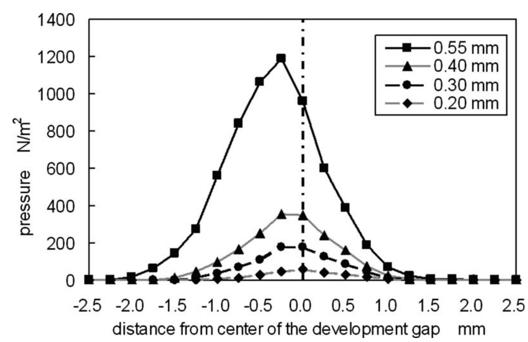

Figure 23. Calculated normal pressure that comes in contact with the photoreceptor drum (parameter: thickness of the layer of supplied carrier particles).

exerted on the photoreceptor. The distribution of the averaged particle density is almost symmetrical with respect to the center of the development gap; however, it is slightly high at the outlet side of the development area; probably because of the friction between the chains and the photoreceptor. The averaged particle density is inversely proportional to the square of the diameter of the particles. Although the total pressure exerted on the photoreceptor is almost independent of the diameter of the carrier particles, as shown in Fig. 18, the differential force exerted by individual chains is small and distributes dense in the case of small particles; on the other hand, it is large and distributes rough in the case of large particles. This suggests that small carrier particles are advantageous in preventing any disturbances in the images developed on the photoreceptor.

In order to confirm this hypothesis, dot images of toner particles (shown in Figure 21) were developed on an actual photoreceptor drum for carrier particles with the different diameters and observed by a microscope camera. It was apparent that high-quality images without scattering of the toner particles could be obtained using small carrier particles.

Effect of the Amount of Carrier Particles Supplied to the Gap

The effect of the thickness of the layer of supplied carrier particles on the development area is investigated. The amount of carrier particles supplied to the development area is controlled by a doctor blade in the actual instrument. The calculated results of the slip speed, normal pressure, and density of the chains that come in contact with the photoreceptor are shown in Figures 22–24, respectively. The nip is long when the thickness of the supplied carrier layer is high; however, the basic feature that the spring-back of the chains takes place behind the development area is not affected by the amount of supplied carrier particles, as can be seem in Fig. 22. On the other hand, the normal pressure and the

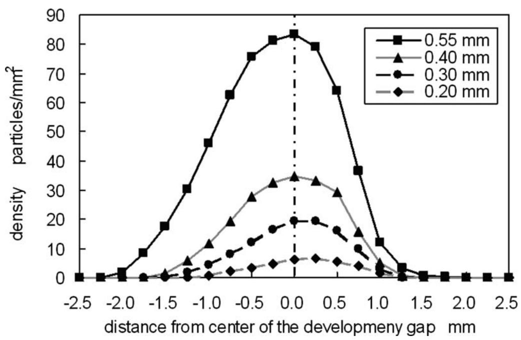

Figure 24. Density of particles that comes in contact with photoreceptor drum (parameter: thickness of the layer of supplied carrier particles).

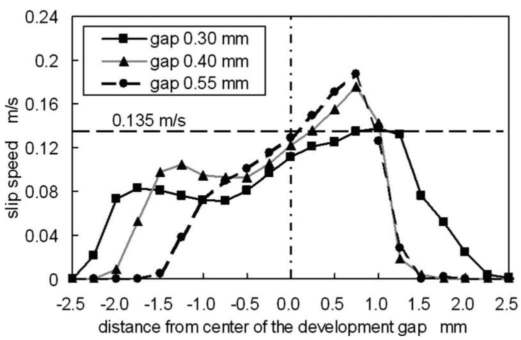

Figure 25. Calculated slip speed of the brush that comes in contact with the photoreceptor drum (parameter: gap).

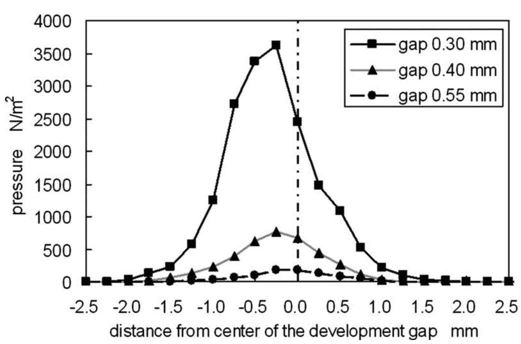

Figure 26. Calculated normal pressure exerted by the brush on the photoreceptor drum (parameter: gap).

density of the chains that come in contact with the photoreceptor increase with the thickness of the layer of supplied carrier particles. In particular, when the thickness exceeds the threshold of 0.4–0.55 mm, the pressure and density increase drastically. The gap between the doctor blade and the photoreceptor drum must be determined by taking these results into consideration.

Effect of Development Gap

Finally, the effect of the development gap on the behavior of the brush is investigated. Figures 25–27 show the calculated results. These results are similar to those shown in Figs. 22–24, respectively. This means that the brush dynamics in the large doctoring gap is almost equivalent to that of the small development gap, although the effect of the latter on the behavior of the brush is larger than the former. The reason of the equivalency is simply that a large amount of carrier particles is supplied to the development area, if the doctoring gap is large.

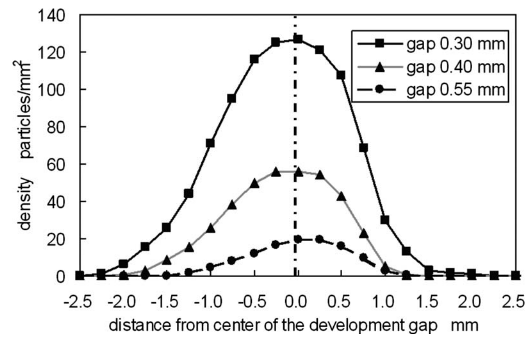

Figure 27. Density of particles that come in contact with photoreceptor drum (parameter: gap).

CONCLUDING REMARKS

Statics and dynamics of the magnetic brush in a two-component development system in electrophotography have been investigated by carrying out a model experiment, direct observations with a high-speed microscope camera, and numerical calculations based on the improved DEM. The calculated results agree reasonably well with the experimental observations. Although the experimental means are restricted to measure integrated quantities, the calculation method can be utilized to evaluate a detailed dynamic and differential performance. The following characteristics have been clarified by these experiments and numerical calculations:

(1) At the inlet of the development area, the magnetic carrier particle chains became parallel to the magnetic field, come in contact with the photoreceptor drum, and are depressed by the drum. The brush is depressed to backward before the chains reach the center of the development gap and spring just before the chains become free. The spring-back of the chains to their normal states behind the development area appears to cause a stripe defect of the toner images developed on the photoreceptor if the force exerted by the brush on the photoreceptor is very high. The slip speed is independent of the diameter of the carrier particles.

(2) The friction force exerted by the brush on the photoreceptor drum increases in accordance with the increase in the magnetic flux density and decreases with an increase in the brush length; however, the diameter of the particles does not affect the total force.

(3) Although the total force exerted on the photoreceptor is almost independent of the diameter of the carrier particles, the differential force exerted by individual chains is small and distributes dense in the case of small particles; on the other hand, it is large and distributes rough in the case of large particles. Small carrier particles are advantageous in preventing any disturbances in the images developed on the photoreceptor.

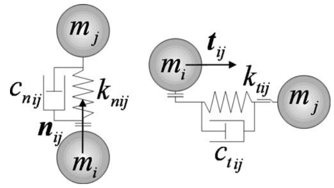

Figure A1. Voigt model for calculating contact force of particles.

(4) The friction force and the density of chains that come in contact with the photoreceptor drum are large when the doctoring gap is large or the development gap is small. When these parameters exceed the threshold, the pressure and the density increase drastically. The gap between the doctor blade and the photoreceptor drum must be determined so that the amount of carrier particles supplied to the development area is moderate.

These experimental and numerical results are used for the improvement of the two-component development system in electrophotography.

ACKNOWLEDGMENT

This study was supported by Samsung Yokohama Research Institute (SYRI). SYRI provided the prototype machine, carrier particles, and measured magnetic flux density data.

APPENDIX: IMPROVED THREE-DIMENSIONAL DEM

DEM is one of the most popular and reliable simulation methods for the numerical analysis of particle dynamics. The following motion equations are solved for each particle j with six degrees of freedom including rotations:[3]

$$m_j \ddot{\boldsymbol{u}}_j = \boldsymbol{F}_j, \quad I_j \ddot{\boldsymbol{\varphi}}_j = \boldsymbol{M}_j, \tag{A1}$$

where m_j, $\boldsymbol{u}_j(=x_j, y_j, z_j)$, I_j, $\boldsymbol{\varphi}_j(=\varphi_{xj}, \varphi_{yj}, \varphi_{zj})$, $\boldsymbol{F}_j$, and $\boldsymbol{M}_j$ are mass, displacement vector, moment of inertia, rotation angle, applied force vector, and moment applied to a particle j, respectively. In this study, mechanical interaction force, magnetic force, air drag, and gravitational force are included in the applied force and momentum.

The mechanical interaction force in the normal and tangential directions is estimated based on Voigt model shown in Figure A1 from Hertzian contact theory and Mindlin contact theory, respectively. The normal force $\boldsymbol{F}_{Cnij}$ from the ith particle to the jth particle is

$$\boldsymbol{F}_{Cnij} = -k_{nij} |\boldsymbol{\delta}_{nij}|^{3/2} \boldsymbol{n}_{ij} - (c_{nij} \boldsymbol{v}_{ij} \cdot \boldsymbol{n}_{ij}) \boldsymbol{n}_{ij}, \tag{A2}$$

where k_{nij} is the spring constant based on the Hertzian contact theory; $|\boldsymbol{\delta}_{nij}|$ is the contact deformation; $\boldsymbol{n}_{ij}$ is the normal unit vector from the center of particle i to j; c_{nij} is the damping constant, and $\boldsymbol{v}_{ij}$ is the relative velocity of particle i to j. The first term of Eq. (A2) is the static reaction force and the second term of Eq. (A2) is the damping force,

$$k_{nij} = \frac{4}{3} \sqrt{\frac{r_i r_j}{r_i + r_j}} \left(\frac{1-\nu_i^2}{E_i} + \frac{1-\nu_j^2}{E_j} \right)^{-1},$$

$$c_{nij} = \alpha \sqrt{\frac{m_i m_j}{m_i + m_j} k_{nij}} |\boldsymbol{\delta}_{nij}|^{1/4}, \tag{A3}$$

where r is the radius of particle; ν is Poisson's ratio; E is Young's modulus, and α is the coefficient of restitution. In the case of no slip, the tangential force $\boldsymbol{F}_{Ctij}$ from the ith particle to the jth particle consists of the static reaction force and damping force,

$$\boldsymbol{F}_{Ctij} = -k_{tij} \boldsymbol{\delta}_{tij} - c_{tij} \boldsymbol{v}_{tij}, \tag{A4}$$

$$k_{tij} = 8 \sqrt{\frac{r_i r_j}{r_i + r_j}} \left(\frac{2-\nu_i}{G_i} + \frac{2-\nu_j}{G_j} \right)^{-1} |\delta_{nij}|^{1/2},$$

$$c_{tij} = \alpha \sqrt{\frac{m_i m_j}{m_i + m_j} k_{tij}}, \tag{A5}$$

where G is the modulus of rigidity. On the other hand, if the slip takes place, the tangential force is limited by the friction force,

$$\boldsymbol{F}_{Ctij} = -\mu_d |k_{tij} \boldsymbol{\delta}_{tij}| \frac{\boldsymbol{v}_t}{|\boldsymbol{v}_t|}, \tag{A6}$$

where μ_d is the friction coefficient. The moment $\boldsymbol{M}_{Cij}$ from the ith particle to the jth particle consists of the contact torque [the first term in the right-hand side of Eq. (A7)] and the rotational friction [the second term in the right-hand side of Eq. (A7)],

$$\boldsymbol{M}_{Cij} = r_j \boldsymbol{n}_{ij} \times \boldsymbol{F}_{Ctij} - r_j \mu_j |\boldsymbol{F}_{Cnij}| \frac{\dot{\boldsymbol{\varphi}}_j}{|\dot{\boldsymbol{\varphi}}_j|}, \tag{A7}$$

where μ_d is the rotational friction coefficient.

The magnetic force $\boldsymbol{F}_{mj}$ and rotational moment $\boldsymbol{M}_{mj}$ of the jth particle with the magnetic moment $\boldsymbol{p}_j$ are given by the following expressions, under the assumption that each particle behaves as a magnetic dipole placed at the center of the magnetized particle:

$$\boldsymbol{F}_{mj} = (\boldsymbol{p}_j \cdot \nabla) \boldsymbol{B}_j, \quad \boldsymbol{M}_{mj} = \boldsymbol{p}_j \times \boldsymbol{B}_j. \tag{A8}$$

The magnetic dipole moment $\boldsymbol{p}_i$ and magnetic flux density $\boldsymbol{B}_i$ at the position of the ith particle are

$$\boldsymbol{B}_j = \boldsymbol{B}'_j + \sum_{\substack{k=1 \\ j \neq k}}^{N} \boldsymbol{B}_{kj}, \tag{A9}$$

$$\boldsymbol{p}_j = \frac{4\pi}{\mu_0} \frac{\mu - 1}{\mu + 2} r_j^3 \boldsymbol{B}_j, \tag{A10}$$

where N is the number of particles; μ_0 is the magnetic permeability of free space, and μ is the relative permeability of the particles. The first term on the right-hand side of Eq. (A9) is the applied magnetic field generated by the magnetic roller and the second term is the field at the jth particle due to the dipoles of the remaining $N-1$ particles. $\boldsymbol{B}_{kj}$ is given by

$$\boldsymbol{B}_{kj}=\frac{\mu_0}{4\pi}\left(\frac{3\boldsymbol{p}_k\cdot\boldsymbol{r}_{kj}}{|\boldsymbol{r}_{kj}|^5}\boldsymbol{r}_{ki}-\frac{\boldsymbol{p}_k}{|\boldsymbol{r}_{kj}|^3}\right), \tag{A11}$$

where $\boldsymbol{r}_{kj}$ is the position vector from the kth to the jth particle. The magnetic force is determined by solving Eqs. (A9)–(A11) simultaneously and by substituting the calculated results of $\boldsymbol{p}_j$ and $\boldsymbol{B}_j$ in Eq. (A8).

The air drag $\boldsymbol{F}_a$ and gravitational force $\boldsymbol{F}_g$ are calculated by the following equations.

$$\boldsymbol{F}_{gj}=-6\pi\eta r_j\dot{\boldsymbol{u}}_j,\quad \boldsymbol{F}_{gj}=m_j\boldsymbol{g}, \tag{A12}$$

where η is the viscosity of air and $\boldsymbol{g}$ is the gravitational acceleration.

Periodical boundary conditions are used to reduce the calculation time. Under these conditions, the kinetics of virtually infinite number of particles can be studied with actually a small number of particles, and thus, the calculation time can be reduced. In addition, chain formation can be studied in a realistic manner under these boundary conditions. If the calculations are conducted in a closed box, the chains magnetically repel one another; hence, the particles are imposed on the wall, as shown in Figure A2 (left pair).

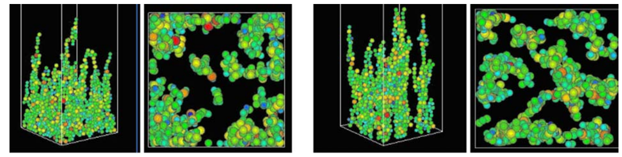

Figure A2. Simulated magnetic brushes with and without periodic boundary conditions.

The repulsion of the chains can be prevented by imposing the periodical boundary conditions, as shown in Fig. A2 (right pair).

REFERENCES

[1] E. M. Williams, *The Physics and Technology of Xerographic Processes* (Krieger, Huntington, NY, 1993).

[2] L. B. Schein, *Electrophotography and Development Physics*, 2nd ed. (Laplacian Press, CA, 1996).

[3] K. Hirakura and H. Kawamoto, *Electrophotography–Process and Simulation* (Tokyo Denki University Press, Tokyo, 2008).

[4] R. S. Paranjpe and H. G. Elrod, "Stability of chains of permeable spherical beads in an applied magnetic field", J. Appl. Phys. **60**, 418–422 (1986).

[5] N. Nakayama, H. Kawamoto, S. Yamada, and A. Sasakawa, "Statics of electromagnetic bead chain in electromagnetic field", *Proc. IS&T's NIP18: International Conference on Digital Printing Technologies* (IS&T, Springfield, VA, 2002), pp. 742–747.

[6] N. Nakayama, H. Kawamoto, and S. Yamada, "Resonance frequency and stiffness of magnetic bead chain in magnetic field", J. Imaging Sci. Technol. **47**, 408–417 (2003).

[7] H. Kawamoto, M. Teshima, and H. Takahashi, "Formation of magnetic particle chains in ultra high magnetic field", J. Advanced Mechanical Design, Systems, and Manufacturing **1**, 669–680 (2007).